Simulating human sleep spindle MEG and EEG from ion channel and circuit level dynamics

Rosen[1,*], B.Q., Krishnan[2,*] G.P., Sanda[2,3], P., Komarov[2], M., Sejnowski[1,4], T., Rulkov[5], N., Bazhenov[1,2,^] ,M., Halgren[1,6,7,^], E.
*co-first ^co-senior

1. Neurosciences Graduate Program, University of California, San Diego, La Jolla CA
2. Department of Medicine, University of California, San Diego, La Jolla CA
3. Institute of Computer Science, Czech Academy of Sciences, Prague, Czech Republic
4. The Salk Institute, La Jolla CA
5. BioCiruits Institute, University of California, San Diego, La Jolla CA
6. Department of Radiology, University of California, San Diego, La Jolla CA
7. Department of Neurosciences, University of California, San Diego, La Jolla CA

Abstract

Background
Although they form a unitary phenomenon, the relationship between extracranial M/EEG and transmembrane ion flows is understood only as a general principle rather than as a well-articulated and quantified causal chain.

Method
We present an integrated multiscale model, consisting of a neural simulation of thalamus and cortex during stage N2 sleep and a biophysical model projecting cortical current densities to M/EEG fields. Sleep spindles were generated through the interactions of local and distant network connections and intrinsic currents within thalamocortical circuits. 32,652 cortical neurons were mapped onto the cortical surface reconstructed from subjects' MRI, interconnected based on geodesic distances, and scaled-up to current dipole densities based on laminar recordings in humans. MRIs were used to generate a quasi-static electromagnetic model enabling simulated cortical activity to be projected to the M/EEG sensors.

Results
The simulated M/EEG spindles were similar in amplitude and topography to empirical examples in the same subjects. Simulated spindles with more core-dominant activity were more MEG weighted.

Comparison with Existing Methods
While previous models lacked either spindle-generating thalamic neural dynamics or whole head biophysical modeling, the framework presented here is the first to simultaneously capture these disparate scales simultaneously.

Conclusions
This multiscale model provides a platform for the principled quantitative integration of existing information relevant to the generation of sleep spindles, and allows the

implications of future findings to be explored. It provides a proof of principle for a methodological framework allowing large-scale integrative brain oscillations to be understood in terms of their underlying channels and synapses.

Keywords
MEG, EEG, Forward Model, Sleep, Spindle, Thalamocortical

1. Introduction

Magnetoencephalography (MEG) and electroencephalography (EEG, together M/EEG), are complementary, non-invasive, instantaneous, and clinically essential, measures of human neural activity. M/EEG are measured as global brain activities, but are known to ultimately arise from channel currents, at a spatial scale ~8 orders of magnitude smaller (Cohen, 2017). The causal chain which leads to M/EEG can be divided into two linked domains: (1) the biophysical propagation of electromagnetic fields after summating and cancelling under anatomical constraints; and (2) the neurobiology of large networks of active neurons whose ionic currents generate these fields. Here we present an initial effort to traverse the spatial scales by integrating simulations of large networks of neurons with biophysical models of electromagnetic propagation, informed by non-invasive imaging and invasive recordings in humans, as well as decades of work in animal models.

Ion movements through ligand- and voltage-gated transmembrane channels result in current flows which are influenced by the intrinsic channel properties of each neuron and the activity of the network. These currents flow through intracellular and extracellular spaces to form complete circuits, restricted by cellular membranes, and thus microscopic cellular anatomy (Einevoll et al., 2013). Currents cancel and summate locally with those of other neurons in the same cortical column, producing a net current which can be expressed as a multipole expansion (Nunez and Srinivasan, 2009). At a distance, the dipolar term predominates, and the local contribution is typically expressed as a current dipole moment. Before reaching the sensors, current dipole moments from different columns cancel and summate mesoscopically with other columns depending on their relative position and orientation in the highly folded cortical surface, and the covariance and phase synchrony of their magnitudes over time (Ahlfors et al., 2010a, 2010b; Irimia et al., 2012; Linden et al., 2011). Ultimately, the signal at each M/EEG sensor is the result of the complex cancellation and summation of microscopic synaptic and intrinsic currents from the many thousands or millions of neurons contributing to any single sensor's leadfield.

Transmembrane currents are the result of spontaneous or evoked neural activity, which can be modeled computationally with various degrees of realism, balancing accuracy at the individual cell level against the quantity of neurons that comprise the simulated network. In the current study, we focus on a model for stage 2 of non-rapid eye movement sleep (N2) which is characterized by spontaneous sleep spindles. Sleep spindles manifest in normal M/EEG as spontaneous bursts of 10-16 Hz activity lasting 0.5-2 s in and are thought to be important for memory consolidation (Andrillon et al., 2011; Bonjean et al., 2011; Contreras et al., 1996; Dehghani et al., 2011; Diekelmann and Born, 2010; Sejnowski and Destexhe, 2000). A large number of studies in animal models have established the key elements in spindle generation: local circuit interactions between thalamocortical and thalamic reticular nucleus neurons, reinforcing intrinsic rhythmicity from successive activation of the hyperpolarization-activated cation current, I_h (Destexhe et al., 1996; McCormick and Pape, 1990) and low-threshold Ca^{2+} current I_T (Huguenard and McCormick, 1992; Huguenard and Prince, 1992). Secondarily, the thalamocortical and corticothalamic projections play a role in synchronizing and terminating the spindle (Bonjean et al., 2011).

Although the initial circuitry and cellular properties generating spindles are thus in the thalamus, the transmembrane currents that produce the M/EEG are cortical. The thalamocortical projection connecting these structures is comprised of a focal projection to layer 4 (termed the 'core'), and a distributed projection to upper layers (termed the 'matrix') (Jones, 2002, 2001). We found previously that sleep spindles detected in MEG are more numerous and less synchronous than EEG spindles (Dehghani et al., 2011, 2010), and suggested that this may reflect a relatively greater sensitivity of EEG to the matrix and MEG to the core projections (Piantoni et al., 2016). Consistent data has been obtained with laminar recordings showing primary involvement of middle or upper layers in different spindles or parts of spindles (Hagler et al., 2018).

In this report we combine neural and biophysical models to generate M/EEG sleep spindles. The neural model is based on our previous computational modeling including the thalamic and cortical local and distant circuits involved in spindles, including matrix and core (Bonjean et al., 2012; Krishnan et al., 2016, in press). All relevant thalamic ligand- and voltage-gated currents are included. The cortical elements are mapped to 20,484 locations on the ~1 mm resolution cortical surface reconstructed from structural MRI. We have found in previous simulations that this resolution is necessary in order to accurately model the interactions between simultaneously active ECDs in producing M/EEG signals (Ahlfors et al., 2010b). In order to computationally model this large number of elements in cortex we use discrete-time models of neurons, which capture critical features of individual cell dynamics and synapses with difference equations, a map (Rulkov, N.F., Timofeev, I., Bazhenov, 2004).

Empirical sleep M/EEG and structural MRI were collected to provide a basis for model evaluation and simulated neurons were embedded in donor cortical and cranial substrates produced from structural MRI. In our framework, the neural activity of individual persons is modeled, as connections among neurons are derived in part from the cortical geometry of the subject. Microscopic cellular currents are scaled to mesoscopic current dipole moment densities using factors derived from human laminar electrode data. The extracranial electromagnetic fields generated by these mesoscopic sources are derived by quasi-static electromagnetic forward modeling, which accounts for orientation induced summation and cancelation by utilizing high-resolution cortical and cranial geometry. Simulated macroscale extracranial M/EEG fields are compared to empirical non-invasive datasets by means of their topography and amplitude.

The modeling approach employed here, an extension of our earlier work, allows for the currents of the coupled core and matrix networks to be isolated. We find that simulated and empirical spindles have similar topographies and that simulated core-dominant spindles had larger spindle band MEG maxima relative to EEG maxima. More generally, we demonstrate a proof-of-concept for relating microscale neuronal parameters to macroscale M/EEG observations.

2. Materials and Methods

The overall structure of the study is shown in Fig. 1. Two kinds of models were constructed: a Neural Model to compute sleep spindle activity during N2 sleep, based on

the known anatomy and physiology of the thalamus and cortex; and a Biophysical Model to project the activity to the M/EEG sensors. Empirical Measurements were obtained and analyzed to produce Derived Measures, used to specify the models and validate the model: Structural MRI to define the location and orientation of cortical generating dipoles, Laminar recordings to scale of the current dipole moment densities generating spindles, and M/EEG in the same subjects to permit validation of model predictions of amplitude and topography.

2.1. Empirical Data

2.1.1. Participants: MEG, EEG, and Structural MRI data were record for 6 healthy adults, (2 male, ages 20-35) . Data for one additional subject was collected but was excluded from analysis due to poor EEG quality. Written informed consent approved by the institutional review boards of the University of California, San Diego or the Partners Healthcare Network, as appropriate, was obtained for all subjects. A whole-head MEG system with integrated EEG cap (Elekta Neuromag) was used to collect 204 planar gradiometers and 60 EEG channels. The position of the subjects' head within the MEG helmet was monitored using head position indicator (HPI) coils, updated every 15-20 minutes. Each subject's headshape, HPI coil locations, and EEG electrode positions were digitized (Polhemus isotrak). Structural MR images were acquired in a separate session.

2.1.2. M/EEG: M/EEG data were acquired during natural sleep at 1 kHz with a 300 Hz low-pass antialiasing filter. Epochs of stage II non-REM sleep were selected for analysis using standard criteria (Iber et al., 2007). Channels with poor data quality or gross artifacts were excluded by visual inspection. The electrocardiogram artifact was removed with independent component analysis (Delorme and Makeig, 2004).

2.1.3. Structural MRI: High-resolution structural images were acquired with a 1.5 Signa HDx whole body scanner (General Electric). The acquisition protocol consisted of a 3-plane localizer, calibration scan, and a high-resolution T1-weighted MP-RAGE scans (TR = 10.728 s, TE = 4.872 ms, TI = 1000 ms, flip angle = 8 degrees, FOV = 256, 176 sagittal slices, 1 mm isotropic).

2.1.4. Laminar recordings: As described in detail in (Hagler et al., 2018), after obtaining fully informed consent according to the Declaration of Helsinki guidelines as monitored by the local Institutional Review Boards, laminar microelectrodes arrays (Ulbert et al., 2001) were implanted into cortical tissue designated for resection in 5 patients (2 male) undergoing surgical treatment for drug resistant epilepsy. These arrays consisted of twenty-four 0.040 mm diameter contacts with 0.150 mm on-center spacing and were inserted along the surface normal of the cortex. Bipolar referencing of reported laminar potentials yields a depth-resolved measure of potential gradients within and among cortical layers to be recorded simultaneously.

2.2. Derived Measures

2.2.1. Calculation of current dipole moment density scale: The laminar current source density (CSD), in $\mu A/mm^3$, of automatically detected sleep spindles was calculated by estimating the explicit quasi-electrostatic inverse of the laminar potential gradients

(Pettersen et al., 2006). CSD's were scaled by their distance from the center of the array to yield current dipole moments per unit volume, and then integrated over the length of the column to yield current dipole moment densities, in μAmm/mm^2, or nAm/mm^2. As shown in Fig. 2, we found sleep spindle surface current densities have an average maximum spindle-band envelope on the order of 0.1 nAm/mm^2 with considerable variation. These measurements are consistent with physiologically plausible maximum current dipole moment densities (Murakami and Okada, 2015). Therefore, the arbitrarily scaled simulated neural currents (in nA) were divided by the approximate Voronoi area (Meyer et al., 2003) of the cortical patch each represents, then scaled to approximately match in amplitude this surface current dipole moment density, yielding corresponding current dipole moment densities in nAm/mm^2.

2.2.2. *M/EEG spindle topographies:* Empirical and simulated M/EEG time series were band-passed to between 10 and 16 Hz with an 8th order zero-phase IIR filter. The spindle-band complex analytic signal was extracted with the Hilbert transform and its envelope obtained by computing the elementwise modulus of the phasor time series. Spindles were automatically detected on empirical and simulated EEG using previously published methods (Andrillon et al., 2011). In short, the spindle band envelope was smoothed with a 300 ms Gaussian kernel (σ = 40 ms), and then normalized into units of standard deviation. Spindle occurrences were assigned to peaks of at least 2 s.d. and their temporal extent extended from these peaks until the smooth envelope fell below 1 s.d. For each detected spindle, the mean (unnormalized) envelope was computed and these data were interpolated over flattened sensor positions to produce topographic maps of spindle band envelope in a standardized head space (Oostenveld et al., 2011). Grand average maps (Fig. 5) were generated by averaging the mean spindle topographies from all subjects, or simulation runs.

2.2.3. *Core/Matrix index:* The degree of core or matrix character was quantified for each simulated spindle. First, the 10-16 Hz envelopes were computed for the neural model derived current dipole moment density time series for core and matrix layers, using the procedure described for M/EEG analysis above. An index of core vs. matrix character was defined:

$$Core/Matrix\ index = \frac{\sum_{t=1}^{T}\sum_{n=1}^{N}\left|\overrightarrow{s_{(t,n)}^{core}}\right|}{\sum_{t=1}^{T}\sum_{n=1}^{N}\left|\overrightarrow{s_{(t,n)}^{matrix}}\right|} - 1 \qquad [1]$$

where T is the duration of the spindle in samples, N is the total number of cortical current dipole moment densities (20484), and $\vec{s}$ is the 10-16 Hz complex analytic signal. Positive values indicate a stronger core character and negative values indicate a stronger matrix character.

2.3. Biophysical Model

2.3.1. Cortical reconstruction: White-gray matter surfaces were reconstructed from the MR volumes using FreeSurfer (Fischl, 2012). Surfaces were sampled at three resolutions as recursively subdivided icosahedra with 642, 10,242, and 163,842 vertices per hemisphere, wherein lower resolution meshes are nested subsets of higher resolution meshes. These are referred to as ico3, ico5, and ico7 surfaces, respectively, indicating the number of subdivisions. Within each hemisphere the geodesic distance between all pairs

of vertices was computed using the Dijkstra approximation (Balasubramanian et al., 2009) with 13 Steiner nodes.

2.3.2. Forward Model (Cortical current dipole moment densities to M/EEG): The forward model, or gain matrix describing the gradiometer and EEG sensor activity produced by equivalent current dipoles at each ico5 vertex was then computed for each subject's cortex. In addition to the white-gray matter surface, four extra-cortical boundary shells were reconstructed from the segmented (Fischl, 2012) images: gray-matter-cerebral-spinal fluid (CSF), CSF-inner skull, inner skull-outer skull, and outer skull-scalp. While the cranial boundaries consisted of triangular meshes with 5,124 vertices, critically, the cortical mesh was sampled at ~1 mm resolution (327,684 vertices) in order to capture the summation and cancelation of opposed dipoles. The position of these surfaces relative to the EEG sensors and HPI coils was determined by registering the digitized headshape to the outer-scalp surface using non-linear optimization (matlab's fmincon) with manual corrections. The position of these surfaces relative to the gradiometers was computed using the known relative positions between and the surfaces and the HPI coils, and the HPI coils and the gradiometers. The orientation of each dipole was set to the surface normal of the white-gray interface. The quasi-static electromagnetic forward solution was numerically computed using a four shell boundary element model, or BEM (Gramfort et al., 2010; Kybic et al., 2005) , with conductivities of 0.33, 0.0042, 0.022, and 0.33 S/m, for the brain, CSF, skull, and scalp, respectively.

Rows of the resulting gain matrices were multiplied by the approximate Voronoi area (Meyer et al., 2003) of the cortical patch each represents to yield a vertex by sensor forward operator describing the contribution of each cortical patch's current dipole moment density to each gradiometer and voltmeter. Current dipole moment densities resulting from core and matrix system pyramidal neurons were computed independently, summed together, and then multiplied by the forward operator to yield simulated EEG and MEEG gradiometer time series.

Briefly, for the relatively low frequency of biologically relevant signals, electric and magnetic fields become uncoupled and the quasi-static approximations of the Maxwell equations can be used (Nunez and Srinivasan, 2009). Under this regime, the EEG forward model is a numeric solution for voltage, V, given f, the divergence of current density distribution, $\mathbf{J}^{\mathrm{p}}$, in the fundamental Poisson equation:

$$\boldsymbol{\nabla} \cdot (\sigma \boldsymbol{\nabla} V) = f = \boldsymbol{\nabla} \cdot \mathbf{J}^{\mathrm{p}} \qquad [2]$$

where σ is the tissue conductivity, in S/m. Because the cranial tissues are modeled as nested, closed, and piecewise homogenous domains, the integration reduces down to solving a symmetric linear system (Kybic et al., 2005). For MEG, solving for the magnetic field $\mathbf{B}$ requires both the current source distribution $\mathbf{J}^{\mathrm{p}}$ and the previously computed electric field V, and is obtained be evaluating the Biot-Savart law at the boundaries:

$$\mathbf{B}(r) = \frac{\mu_0}{4\pi} \int \left(\mathbf{J}^{\mathrm{p}}(\mathbf{r}') - \sigma \boldsymbol{\nabla} V(\mathbf{r}') \right) \times \frac{\mathbf{r}-\mathbf{r}'}{\|\mathbf{r}-\mathbf{r}'\|^3} d\mathbf{r}' \qquad [3]$$

where $\mathbf{r}$ and $\mathbf{r}'$ are displacements of the current source and magnetometer, respectively, and μ_0 is the vacuum permeability constant. Planar gradiometer leadfields are derived by

differentiating virtual magnetometer, or integration point, leadfields with respect to the length of the gradiometer. See (Gramfort et al., 2010; Kybic et al., 2005) these methods in greater detail.

2.4. Neural Model

2.4.1. Neurons: We used a computational model of a thalamocortical network (Fig 2A) with three layers in cortex, with each layer comprising of excitatory (PY) neurons and inhibitory (IN) neurons. The thalamus consisted of a network of core (specific) and matrix (non-specific) nuclei, each consisting of thalamic relay (TC) and reticular (RE) neurons. A computationally efficient phenomenological model based on difference equation (map-based) model was used for cortical PY and IN cells. We have previously demonstrated that such a map based neuron is computationally efficient and able to reproduce the same response characteristics of conductance based neurons (Bazhenov et al., 2008; Rulkov, N.F., Timofeev, I., Bazhenov, 2004; Rulkov and Bazhenov, 2008) and also capable of generating sleep oscillations (Komarov et al., 2017). The following equation describes the update of the PY neurons in time:

$$x_{t+1} = f_\alpha\left(x_t,\ y_t + \beta I_{syn}\right)$$

$$y_{t+1} = y_t - \mu(x_t + 1) + \mu\,\sigma + \mu * \beta_y I_{syn} \qquad [4]$$

where variable x_t represents the membrane potential of a biological neuron at time t and y_t represent slow varying ion channel dynamics. The parameter μ (=0.0005) describes the change in the slow variable (μ less than 1 lead to slow update of y variable). The parameter β scale the input synaptic currents (I_{syn}) for x variable, with β =0.133. The parameter σ (=0.02) defines the resting potential of the model neuron. The function f_α is given below:

$$f_\alpha\,(x_t, u_t) = \begin{cases} \frac{\alpha}{1-x_t} + u_t, & x \le 0 \\ \alpha + u_t, & 0 < x_t < \alpha + u_t \ \ x_{t-1} \le 0 \\ -1, & x_t \ge \alpha + u_t \ OR\ x_{t-1} > 0 \end{cases} \qquad [5]$$

where u_t is taken as $y_t + \beta\ I_{syn}$ from Eq 1, α (=3.65) is a control parameter which was set to obtain tonic spiking like activity for wide range of input currents. The inhibitory neurons were implemented using only the x variable to capture the fast spiking nature of inhibitory neurons and is described by the following equation:

$$x_{t+1} = f_\alpha\left(x_t, y^* + \beta\ I_{syn}\right) \qquad [6]$$

where, y^*=-2.90 with the same f_α function as Eq 2 with α =3.8 and β =0.05.

The thalamic TC and RE cells were modeled as conductance based neurons, described by the following equation:

$$C_m \frac{dV}{dt} = -\,g_{leak}\left(V - E_{leak}\right) - I_{int} - I_{syn} \qquad [7]$$

where the membrane capacitance, C_m, is equal to 1 μF/cm^2, non-specific (mixed Na^+ and Cl^-) leakage conductance, g_{leak}, is equal to 0.0142 mS/cm^2 for TC cells and 0.05 mS/cm^2

for RE cells, and the reversal potential, E_{leak}, is equal to -70 mV for TC cells and -77 mV for RE cells. I_{int} is the sum of active intrinsic currents, and I_{syn} is the sum of synaptic currents. The area of a RE cell and a TC cell was 1.43×10^{-4} cm^2 and 2.9×10^{-4} cm^2, respectively. RE and TC cells included fast sodium current, I_{Na}, a fast potassium current, I_K, a low-threshold Ca^{2+} current I_T, and a potassium leak current, $I_{KL} = g_{KL}$ (V - E_{KL}), where E_{KL} = -95 mV. In addition, a hyperpolarization-activated cation current, I_h, was also included in TC cells. For TC cells, the maximal conductances are g_K = 10 mS/cm^2, g_{Na}= 90 mS/cm^2, g_T= 2.2 mS/cm^2, g_h = 0.017 mS/cm^2, g_{KL} = 0.0142 mS/cm^2. For RE cells, the maximal conductances are g_K = 10 mS/cm^2, g_{Na} = 100 mS/cm^2, g_T = 2.3 mS/cm^2, g_{leak} = 0.005 mS/cm^2.The expressions of voltage- and Ca^{2+}- dependent transition rates for all currents are given in (Bazhenov et al., 2002; Chen et al., 2012).

2.4.2. Synaptic currents: All the inputs to the map based neurons were described by the

$$\{g_{t+1}^{syn}, d_{t+1}\} = \begin{cases} \{\gamma g_t^{syn} + g_{syn} d_n, (1-\eta) d_n\}, & spike_{pre} \\ \{\gamma g_t^{syn}, 1-(1-\delta)(1-d_n)\},, & otherwise \end{cases} \quad [8]$$

where g_{t+1}^{syn} and d_{t+1} are the synaptic conductance and depression variable for time t+1, $g_{syn}$is the synaptic coupling strength similar to the maximal conductance. The parameter $\gamma = 0.99$ is the decay variable to capture the first order kinetics of the synaptic transmission, $\eta = 0.00005$ is the rate of decay of the depression variable (d). The synaptic currents that are input to all conductance based neurons were described as:

$$\mathrm{I_{syn}} = g_{syn}[O](V - E_{syn}) \quad [9]$$

where $g_{syn}$is the maximal conductance, $[O]$ is the fraction of open channels, and E_{syn} is the reversal potential. In RE and PY cells, reversal potential was 0 mV for AMPA receptors, and -70 mV for GABA-A receptors. For TC cells, the reversal potential was -80 mV for GABA-A receptors, and -95 mV for GABA-B receptors. GABAA, and AMPA synaptic currents were modeled by the first-order activation schemes. GABA-B receptors were modeled by a higher-order reaction scheme that considers the activation of K^+ channels by G-proteins. The equations for all synaptic currents were given in (Timofeev, I., Grenier F., Bazhenov, M., Sejnowski, T.J., Steriade, 2000).

Spontaneous miniature EPSPs and IPSPs were included for the AMPA and GABA-A connections within cortical neurons. The arrival times of miniature EPSPs and IPSPs followed the Poisson process (Stevens, 1993), with time-dependent mean rate $\mu = \log(\frac{t-t_0+T}{T})$ where t is current time and t_0 was timing of the last presynaptic spike and T=50ms.

2.4.3. Synaptic conductance: A detailed network connectivity is shown in Fig 2A. The maximal conductances for various connections were $g_{GABA\text{-}A}$(RE-TC) = 0.045 μS, $g_{GABA\text{-}B}$(RE-TC) = 0.06 μS, $g_{GABA\text{-}A}$(RE-RE) = 0.175 μS; core thalamus: g_{AMPA}(TC-PY) = 0.03 μS, g_{AMPA}(TC-IN) = 0.015 μS; matrix thalamus: g_{AMPA}(TC-PY) = 0.045 μS, g_{AMPA}(TC-IN) = 0.02 μS; connections within each layer (matrix, core and L6) pyramidal neurnons: g_{AMPA}(PY-PY) = 2.5 nS, g_{NMDA}(PY-PY) = 0.4 nS; connection from matrix to core: g_{AMPA}(PY-PY) = 1.5 nS, g_{NMDA}(PY-PY) = 0.1 nS; connection from matrix to L6 : g_{AMPA}(PY-PY) = 2.0 nS, gNMDA(PY-PY) = 0.2 nS; connection from core to matrix:

g_{AMPA} (PY-PY) = 1.5 nS, g_{NMDA}(PY-PY) = 0.1 nS; connection from core to L6: g_{AMPA}(PY-PY) = 2.0 nS, g_{NMDA}(PY-PY) = 0.2 nS; connection from L6 to matrix: g_{AMPA}(PY-PY) = 2.0 nS, g_{NMDA}(PY-PY) = 0.2 nS; connection from L6 to core: g_{AMPA}(PY-PY) = 1.5 nS, gNMDA(PY-PY) = 0.1 nS; connection betwen PY and IN cells for all layers: g_{AMPA}(PY-IN) = 0.05 μS, g_{NMDA}(PY-IN) = 0.4 nS, $g_{GABA\text{-}A}$(IN-PY) = 0.05 μS and connection from core and L6 cells to thalamic neurons: g_{AMPA}(PY-TC) = 0.025 μS, g_{AMPA}(PY-RE) = 0.045 μS.

2.4.4. Network connectivity: For each subject's donor cortex, one pyramidal neuron was simulated for each vertex in the ico5 mesh (10,242 vertices per hemisphere) for each of layers matrix, core, and L6. The ico3 mesh was populated with inhibitory and thalamic neurons at each of 642 vertices per hemisphere. For all intra-hemispheric synapses, connectively was established by comparing synapse-specific fan-out radii to the geodesic distance between vertices on the ico7 cortex (163,842 vertices per hemisphere), see Fig. 3B. Inter-hemispheric synapses were threaded between homologously located neurons in 85% of cases and the remaining connections were made between randomly located neurons. Fig. 4B shows simulated current on an inflated cortex at a single time point for the core and matrix neurons.

3. Results

We designed a thalamocortical network model that combined the detailed laminar connectivity with the network connectivity of the whole brain based on MRI reconstructions. Using this approach we demonstrate the feasibility of connecting the cellular level activity with the macroscopic activity seen in EEG/MEG. We used a difference equation or map-based model for cortical neurons, which has the computational efficiency necessary for simulating large-scale networks and conductance based neuronal models for the thalamic network, as required to simulate specific patterns of electrical activity.

The state of the network was set to be stage 2 sleep state by modifying the intrinsic and synaptic currents to mimic the level of low acetylcholine, nor-epinephrine and histamine similar to our previous work. In this state, the network spontaneously generated electrical activity similar to our previous studies (Bazhenov et al., 2000; Bonjean et al., 2011; Krishnan et al., 2016) consisting of multiple randomly occurring spindle events involving thalamic and cortical neuronal populations. The cortical and thalamic neurons in both the core and matrix system had elevated and synchronized firing, during such spindle events (Fig 3A) consistent with previous in-vivo experimental recordings (Steriade et al., 1993). Next, we applied a forward modeling technique that used results from the large-scale simulations of thalamocortical network to simulate EEG and MEG signals.

Microscopic transmembrane currents were scaled up to mesoscopic patch current dipole moment densities, a quantity corresponding to the dipole moment per unit area, This was accomplished by in two steps: scaling these currents by the cortical patch area represented by each column, then scaling these current densities to be consistent with empirical spindle current dipole moment densities recorded from human laminar microelectrode data and physiologically plausible maximum current dipole moment

densities (Murakami and Okada, 2015).

We found that the model was able to simulate essential elements of empirical M/EEG. Grand average topographies of simulated and experimental data, shown in fig. 5, are qualitatively similar to experimental ones. The simulated M/EEG also reproduces the magnitude of the empirical M/EEG with average spindle topography maxima (mean ± s.d. across all subjects or model runs) of 56.8 ± 12.6 fT/cm and 49.4 ± 13.4 fT/cm, $p = 0.93$, for simulated and empirical MEG, respectively, and 8.7 ± 0.8 μV and 10.7 ± 2.0 μV, $p = 0.96$, for simulated and empirical EEG, see fig. 6 A. For simulated spindles, the relative contributions of the core and matrix systems to current dipole moment densities was quantified and, as shown in fig. 6 B, we found this index to correlate with the ratio of derived MEG vs. EEG maxima (Pearson's $r = 0.24$, $p = 0.019$).These data are consistent with the hypothesis that MEG gradiometer recordings are more sensitive to core system neurons when compared to EEG recordings which are biased towards the matrix system. However, other factors, including individual differences, could also explain these results, and more focused studies are needed.

4. Discussion

In this study, we developed a computationally efficient large-scale hybrid thalamocortical model of sleep spindles with cortical patches that were realistically arranged in space based on the structural MRI data. Using the output of the model simulation, we obtained the activity which would be seen in EEG and MEG sensors. The spatial and temporal features of the M/EEG derived from the model were similar to those found in empirical recordings in healthy subjects, when using their brain and head anatomy to define the projection from cortex to M/EEG, thereby validating our approach. In addition, we found evidence to support the previous hypothesis (Bonjean et al., 2011; Dehghani et al., 2010) that EEG activity during spindles reflects the activity of the superficial matrix layers while MEG is more sensitive to core neurons. Thus, using this approach, we demonstrate the viability of an integrated model for the generation of EEG/MEG, proceeding from ionic and synaptic activity, through local and distant networks, whose currents are then passed through a realistic biophysical model to generate MEEG fields that correspond to empirical recordings, a foundational problem in neuroimaging.

At its base, our study used a realistic computational model at level of intrinsic and synaptic transmembrane currents to simulate EEG/MEG. Ritter et al. (Ritter et al., 2013) have demonstrated modeled EEG signals from population based neural mass models of cortical activity projected to extracranial sensors. While such models could reproduce the spectrogram of EEG, they do not explicitly resolve activity at the level of individual neuron's ionic or synaptic currents. This becomes critical when trying to leverage information from extensive intracellular and direct recordings of cortical and thalamic activity, e.g. (Steriade and Timofeev, 2003). Costa and colleagues (Costa et al., 2016) included some of these details in their neural mass model, but their biophysical modeling of EEG was rudimentary, only considering an anatomically and physiologically implausible point source.

Extracranial M/EEG fields generated by a cortical dipole depend not only on it location

and the magnitude of its moment, but are also highly dependent on the extent of spatial-temporal synchrony with other dipoles across the cortex and their relative orientations (Ahlfors et al., 2010a; Lutkenhoner, 2003). Dipoles are created by the post-synaptic currents of pyramidal neurons aligned and are thus perpendicular to cortical surface (Lopes Da Silva, 2004; Nunez and Srinivasan, 2009). Thus, synchronous dipoles with opposed orientations, such as those on opposite side of the sulcal walls, will cancel each other out. If fact, the majority of the typical MEG signal is canceled because of this phenomena (Ahlfors et al., 2010b; Lutkenhoner, 2003). Therefore, computing the quasi-static electromagnetic forward solution for a high-resolution cortical mesh is critical for capturing the effects of dipole cancelation and summation. Indeed, our surface geometry was sampled at ~1 mm resolution or 327,684 sources.

The leadfields of MEG gradiometers are smaller than those of EEG, even though MEG sensors are typically further away from the generators (Irimia et al., 2012). This is primarily because EEG is smeared by the skull and cranial tissues whereas MEG these structures are mostly transparent to MEG (Hämäläinen and Ilmoniemi, 1994) and also because the sources of bipolar gradients, such as MEG gradiometers are more focal than distantly reference scalp EEG. It is likely that intermodal differences in leadfield extent render the instruments differentially sensitive to phenomena with broad or focal spatial extents (Dehghani et al., 2010). The core and matrix thalamocortical pathways (Jones, 2002, 2001), which innervate subgranular neurons sparsely and superficial neurons broadly, respectively, can explain differences in the spatial extent of MEG and EEG spindles by attributing the MEG activity to the core and EEG activity to the matrix (Bonjean et al., 2012). In this study we found evidence for this prediction by deriving the EEG and MEG activity from a multi-layer cortical network that includes the thalamus. We found that derived M/EEG activity is more MEG weighted for core dominant spindles.

Given the scale and complexity of the system that our framework attempts to emulate, it unsurprising that its limitations are numerous. Most notably, this model does not take into account functional specialization or cytoarchitectonic differentiation among cortical regions, including hemispheric laterality. Future developments of our approach will incorporate structural and functional connectivity maps and parcellation, e.g. (Burt et al., 2017; Smith et al., 2013; van den Heuvel and Sporns, 2013). The scaling from single neuron current to patch current dipole moment density, while empirically grounded, is approximate in magnitude and restrictive in orientation. Subcortical areas other than the thalamus are not included in the models. While the direct contribution of these areas to extracranial M/EEG is minimal (Cohen et al., 2011), many, e.g. the nucleus basalis and hippocampus, may play critical roles in the timing, extent, amplitude and propagation of cortical activity during spindling. Future iterations of the model will address these limitations.

A more comprehensive understanding of the relationship between neurobiology, local field potentials, and non-invasive M/EEG might plausibly improve the diagnostic power of the latter techniques. Understanding the forward model from ion channel dynamics to M/EEG is the first step towards developing a principled inverse solution that maps M/EEG responses to clinically and physiologically relevant human *in vivo* molecular measures.

Acknowledgements

This research was supported by NIH grants R01-EB009282, R01-MH099645-04, and T32-NS061847, as well as ONR grant N00014-16-1-2829. We thank Nima Dehghani, Donald Hagler, and Sergey Gratiy for their contributions to the empirical data, as well as our human subjects for their participation.

References

Ahlfors, S.P., Han, J., Belliveau, J.W., Hämäläinen, M.S., 2010a. Sensitivity of MEG and EEG to source orientation. Brain Topogr. 23, 227–232. https://doi.org/10.1007/s10548-010-0154-x

Ahlfors, S.P., Han, J., Lin, F.H., Witzel, T., Belliveau, J.W., Hämäläinen, M.S., Halgren, E., 2010b. Cancellation of EEG and MEG signals generated by extended and distributed sources. Hum. Brain Mapp. 31, 140–149. https://doi.org/10.1002/hbm.20851

Andrillon, T., Nir, Y., Staba, R.J., Ferrarelli, F., Cirelli, C., Tononi, G., Fried, I., 2011. Sleep Spindles in Humans: Insights from Intracranial EEG and Unit Recordings. J. Neurosci. 31, 17821–17834. https://doi.org/10.1523/JNEUROSCI.2604-11.2011

Balasubramanian, M., Polimeni, J.R., Schwartz, E.L., 2009. Exact geodesics and shortest paths on polyhedral surfaces. IEEE Trans. Pattern Anal. Mach. Intell. 31, 1006–1016. https://doi.org/10.1109/TPAMI.2008.213

Bazhenov, M., Rulkov, N.F., Timofeev, I., 2008. Effect of synaptic connectivity on long-range synchronization of fast cortical oscillations. J. Neurophysiol. 100, 1562–1575. https://doi.org/10.1152/jn.90613.2008

Bazhenov, M., Timofeev, I., Steriade, M., Sejnowski, T., 2000. Spiking-bursting activity in the thalamic reticular nucleus initiates sequences of spindle oscillations in thalamic networks. J. Neurophysiol. 84, 1076–1087.

Bazhenov, M., Timofeev, I., Steriade, M., Sejnowski, T.J., 2002. Model of thalamocortical slow-wave sleep oscillations and transitions to activated States. J. Neurosci. 22, 8691–8704. https://doi.org/22/19/8691 [pii]

Bonjean, M., Baker, T., Bazhenov, M., Cash, S., Halgren, E., Sejnowski, T., 2012. Interactions between Core and Matrix Thalamocortical Projections in Human Sleep Spindle Synchronization. J. Neurosci. 32, 5250–5263. https://doi.org/10.1523/JNEUROSCI.6141-11.2012

Bonjean, M., Baker, T., Lemieux, M., Timofeev, I., Sejnowski, T., Bazhenov, M., 2011. Corticothalamic Feedback Controls Sleep Spindle Duration In Vivo. J. Neurosci. 31, 9124–9134. https://doi.org/10.1523/JNEUROSCI.0077-11.2011

Burt, J.B., Demirtas, M., Eckner, W.J., Navejar, N.M., Ji, J.L., Martin, W.J., Bernacchia, A., Anticevic, A., Murray, J.D., 2017. Hierarchy of transcriptomic specialization across human cortex captured by myelin map topography. bioRxiv 199703. https://doi.org/10.1101/199703

Chen, J.-Y., Chauvette, S., Skorheim, S., Timofeev, I., Bazhenov, M., 2012. Interneuron-mediated inhibition synchronizes neuronal activity during slow oscillation. J. Physiol. 590, 3987–4010. https://doi.org/10.1113/jphysiol.2012.227462

Cohen, M.X., 2017. Where Does EEG Come From and What Does It Mean? Trends Neurosci. 40, 208–218. https://doi.org/10.1016/j.tins.2017.02.004

Cohen, M.X., Cavanagh, J.F., Slagter, H.A., 2011. Event-related potential activity in the

basal ganglia differentiates rewards from nonrewards: Temporospatial principal components analysis and source localization of the feedback negativity: Commentary. Hum. Brain Mapp. 32, 2270–2271. https://doi.org/10.1002/hbm.21358
Contreras, D., Destexhe, A., Sejnowski, T.J., Steriade, M., 1996. Control of spatiotemporal coherence of a thalamic oscillation by corticothalamic feedback. Science (80-.). 274, 771–774. https://doi.org/10.1126/science.274.5288.771
Costa, M.S., Weigenand, A., Ngo, H.V. V, Marshall, L., Born, J., Martinetz, T., Claussen, J.C., 2016. A Thalamocortical Neural Mass Model of the EEG during NREM Sleep and Its Response to Auditory Stimulation. PLoS Comput. Biol. 12, 1–20. https://doi.org/10.1371/journal.pcbi.1005022
Dehghani, N., Cash, S.S., Halgren, E., 2011. Emergence of synchronous EEG spindles from asynchronous MEG spindles. Hum. Brain Mapp. 32, 2217–2227. https://doi.org/10.1002/hbm.21183
Dehghani, N., Cash, S.S., Rossetti, A.O., Chen, C.C., Halgren, E., 2010. Magnetoencephalography Demonstrates Multiple Asynchronous Generators During Human Sleep Spindles. J Neurophysiol 104, 179–188. https://doi.org/10.1152/jn.00198.2010
Delorme, A., Makeig, S., 2004. EEGLAB: an open source toolbox for analysis of single-trial EEG dynamics including independent component analysis. J. Neurosci. Methods 134, 9–21.
Destexhe, A., Contreras, D., Steriade, M., Sejnowski, T.J., Huguenard, J.R., 1996. In vivo, in vitro, and computational analysis of dendritic calcium currents in thalamic reticular neurons. J. Neurosci. 16, 169–85. https://doi.org/10.3961/jpmph.2008.41.6.365
Diekelmann, S., Born, J., 2010. The memory function of sleep. Nat. Rev. Neurosci. 11, 114–126. https://doi.org/10.1038/nrn2762
Einevoll, G.T., Kayser, C., Logothetis, N.K., Panzeri, S., 2013. Modelling and analysis of local field potentials for studying the function of cortical circuits. Nat. Rev. Neurosci. 14, 770–785. https://doi.org/10.1038/nrn3599
Fischl, B., 2012. FreeSurfer. Neuroimage. https://doi.org/10.1016/j.neuroimage.2012.01.021
Gramfort, A., Papadopoulo, T., Olivi, E., Clerc, M., 2010. OpenMEEG: opensource software for quasistatic bioelectromagnetics. Biomed. Eng. Online 9, 45. https://doi.org/10.1186/1475-925X-9-45
Hagler, D.J., Ulbert, I., Wittner, L., Erőss, L., Madsen, J.R., Devinsky, O., Doyle, W., Fabo, D., Cash, S.S., Halgren, E., 2018. Heterogeneous origins of human sleep spindles in different cortical layers. J. Neurosci. 38, 2241–17. https://doi.org/10.1523/JNEUROSCI.2241-17.2018
Hämäläinen, M.S., Ilmoniemi, R.J., 1994. Interpreting magnetic fields of the brain: minimum norm estimates. Med. Biol. Eng. Comput. 32, 35–42. https://doi.org/10.1007/BF02512476
Huguenard, J.R., McCormick, D.A., 1992. Simulation of the currents involved in rhythmic oscillations in thalamic relay neurons. J. Neurophysiol. 68, 1373–1383. https://doi.org/10.1017/CBO9781107415324.004
Huguenard, J.R., Prince, D.A., 1992. A novel T-type current underlies prolonged Ca2+-dependent burst firing in GABAergic neurons of rat thalamic reticular nucleus. J.

Neurosci. 12, 3804–3817. https://doi.org/10.1007/s00401-013-1221-7
Iber, C., Ancoli-Israel, S., Chesson, A., Quan, S., 2007. The AASM Manual for the Scoring of Sleep and Associates Events: Rules, Terminology and Technical Specifications, Sleep (Rochester). https://doi.org/10.1002/ejoc.201200111
Irimia, A., Van Horn, J.D., Halgren, E., 2012. Source cancellation profiles of electroencephalography and magnetoencephalography. Neuroimage 59, 2464–2474. https://doi.org/10.1016/j.neuroimage.2011.08.104
Jones, E.G., 2002. Thalamic circuitry and thalamocortical synchrony. Philos. Trans. R. Soc. B Biol. Sci. 357, 1659–1673. https://doi.org/10.1098/rstb.2002.1168
Jones, E.G., 2001. The thalamic matrix and thalamocortical synchrony. Trends Neurosci. https://doi.org/10.1016/S0166-2236(00)01922-6
Komarov, M., Krishnan, G., Chauvette, S., Rulkov, N., Timofeev, I., Bazhenov, M., 2017. New class of reduced computationally efficient neuronal models for large-scale simulations of brain dynamics. J. Comput. Neurosci. 1–24. https://doi.org/10.1007/s10827-017-0663-7
Krishnan, G.P., Chauvette, S., Shamie, I., Soltani, S., Timofeev, I., Cash, S.S., Halgren, E., Bazhenov, M., 2016. Cellular and neurochemical basis of sleep stages in the thalamocortical network. Elife 5, 1–29. https://doi.org/10.7554/eLife.18607
Krishnan, G.P., Rosen, B.Q., Chen, J.-Y., Muller, L., Sejnowski, T.J., Cash, S.S., Halgren, E., Bazhenov, M., 2017. Thalamocortical and Intracortical Laminar Connectivity Determines Sleep Spindle Properties. bioRxiv 195552. https://doi.org/10.1101/195552
Kybic, J., Clerc, M., Abboud, T., Faugeras, O., Keriven, R., Papadopoulo, T., 2005. A common formalism for the integral formulations of the forward EEG problem. IEEE Trans. Med. Imaging 24, 12–28. https://doi.org/10.1109/TMI.2004.837363
Linden, H., Tetzlaff, T., Potjans, T.C., Pettersen, K.H., Grun, S., Diesmann, M., Einevoll, G.T., 2011. Modeling the spatial reach of the LFP. Neuron 72, 859–872. https://doi.org/10.1016/j.neuron.2011.11.006
Lopes Da Silva, F., 2004. Functional localization of brain sources using EEG and/or MEG data: Volume conductor and source models, in: Magnetic Resonance Imaging. pp. 1533–1538. https://doi.org/10.1016/j.mri.2004.10.010
Lutkenhoner, B., 2003. Magnetoencephalography and its Achilles' heel, in: Journal of Physiology Paris. pp. 641–658. https://doi.org/10.1016/j.jphysparis.2004.01.020
McCormick, D.A., Pape, H.C., 1990. Properties of a hyperpolarization-activated cation current and its role in rhythmic oscillation in thalamic relay neurones. J. Physiol. 431, 291–318. https://doi.org/10.1113/jphysiol.1990.sp018331
Meyer, M., Desbrun, M., Schröder, P., Barr, A.H., 2003. Discrete Differential-Geometry Operators for Triangulated 2-Manifolds. pp. 35–57. https://doi.org/10.1007/978-3-662-05105-4_2
Murakami, S., Okada, Y., 2015. Invariance in current dipole moment density across brain structures and species: Physiological constraint for neuroimaging. Neuroimage 111, 49–58. https://doi.org/10.1016/j.neuroimage.2015.02.003
Nunez, P.L., Srinivasan, R., 2009. Electric Fields of the Brain: The neurophysics of EEG, Electric Fields of the Brain: The neurophysics of EEG. https://doi.org/10.1093/acprof:oso/9780195050387.001.0001
Oostenveld, R., Fries, P., Maris, E., Schoffelen, J.-M., 2011. FieldTrip: Open source

software for advanced analysis of MEG, EEG, and invasive electrophysiological data. Comput. Intell. Neurosci. 2011, 156869. https://doi.org/10.1155/2011/156869
Pettersen, K.H., Devor, A., Ulbert, I., Dale, A.M., Einevoll, G.T., 2006. Current-source density estimation based on inversion of electrostatic forward solution: Effects of finite extent of neuronal activity and conductivity discontinuities. J. Neurosci. Methods 154, 116–133. https://doi.org/10.1016/j.jneumeth.2005.12.005
Piantoni, G., Halgren, E., Cash, S.S., 2016. Spatiotemporal Characteristics of Sleep Spindles Depend on Cortical Location. Neuroimage 146, 236–245. https://doi.org/10.1016/j.neuroimage.2016.11.010
Ritter, P., Schirner, M., McIntosh, A.R., Jirsa, V.K., 2013. The virtual brain integrates computational modeling and multimodal neuroimaging. Brain Connect. 3, 121–145. https://doi.org/10.1089/brain.2012.0120
Rulkov, N.F., Timofeev, I., Bazhenov, M., 2004. Oscillations in Large-Scale Cortical Networks : Map-Based Model. J. Comput. Neurosci. 17, 203–223.
Rulkov, N.F., Bazhenov, M., 2008. Oscillations and synchrony in large-scale cortical network models. J. Biol. Phys. 34, 279–299. https://doi.org/10.1007/s10867-008-9079-y
Sejnowski, T.J., Destexhe, A., 2000. Why do we sleep? Brain Res. 886, 208–223. https://doi.org/10.1016/S0006-8993(00)03007-9
Smith, S.M., Beckmann, C.F., Andersson, J., Auerbach, E.J., Bijsterbosch, J., Douaud, G., Duff, E., Feinberg, D.A., Griffanti, L., Harms, M.P., Kelly, M., Laumann, T., Miller, K.L., Moeller, S., Petersen, S., Power, J., Salimi-Khorshidi, G., Snyder, A.Z., Vu, A.T., Woolrich, M.W., Xu, J., Yacoub, E., Uğurbil, K., Van Essen, D.C., Glasser, M.F., 2013. Resting-state fMRI in the Human Connectome Project. Neuroimage 80, 144–168. https://doi.org/10.1016/j.neuroimage.2013.05.039
Steriade, M., McCormick, D., Sejnowski, T., 1993. Thalamocortical oscillations in the sleeping and aroused brain. Science (80-.). 262, 679–685. https://doi.org/10.1126/science.8235588
Steriade, M., Timofeev, I., 2003. Review Neuronal Plasticity in Thalamocortical Networks during Sleep and Waking Oscillations present in the background electrical activity during the brain-activated states of waking and REM sleep, are also thought to enhance temporal coherence of re. Neuron 37, 563–576. https://doi.org/10.1016/S0896-6273(03)00065-5
Stevens, C.F., 1993. Quantal release of neurotransmitter and long-term potentiation. Cell. https://doi.org/10.1016/S0092-8674(05)80028-5
Timofeev, I., Grenier F., Bazhenov, M., Sejnowski, T.J., Steriade, M., 2000. Origin of Slow Cortical Oscillations in Deafferented Cortical Slabs. Cereb. Cortex 10, 1185–1199. https://doi.org/10.1093/cercor/10.12.1185
Ulbert, I., Halgren, E., Heit, G., Karmos, G., 2001. Multiple microelectrode-recording system for human intracortical applications. J. Neurosci. Methods 106, 69–79. https://doi.org/10.1016/S0165-0270(01)00330-2
van den Heuvel, M.P., Sporns, O., 2013. An Anatomical Substrate for Integration among Functional Networks in Human Cortex. J. Neurosci. 33, 14489–14500. https://doi.org/10.1523/JNEUROSCI.2128-13.2013

Tables

Table 1. Method advantages and limitations

Advantages	Limitations
Quantitatively relates neural and extracranial measures	Lacks detailed modeling of the columnar microstructure
Includes detailed dynamics of thalamic neurons including low-threshold Ca^{2+} currents	Does not account for conduction delays in long distance connections
High resolution biophysical model captures effects of orientation and cancellation in cortical manifold	Example presented does not include areal diversity, but is possible within model framework
Can be use to probe intermodal differences and individual-specific anatomy and sensor configurations	Modeling of interhemispheric connectivity is rudimentary
Produces empirically observed M/EEG amplitudes from biologically plausible current dipole moment densities	White matter tractography not used to inform connectivity, planned for future iterations

Figures and Legends

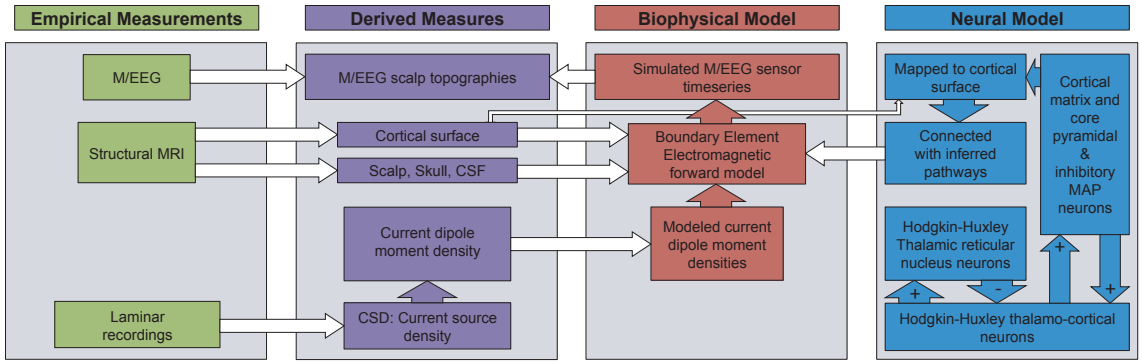

Figure 1. Overall structure of Experiment.

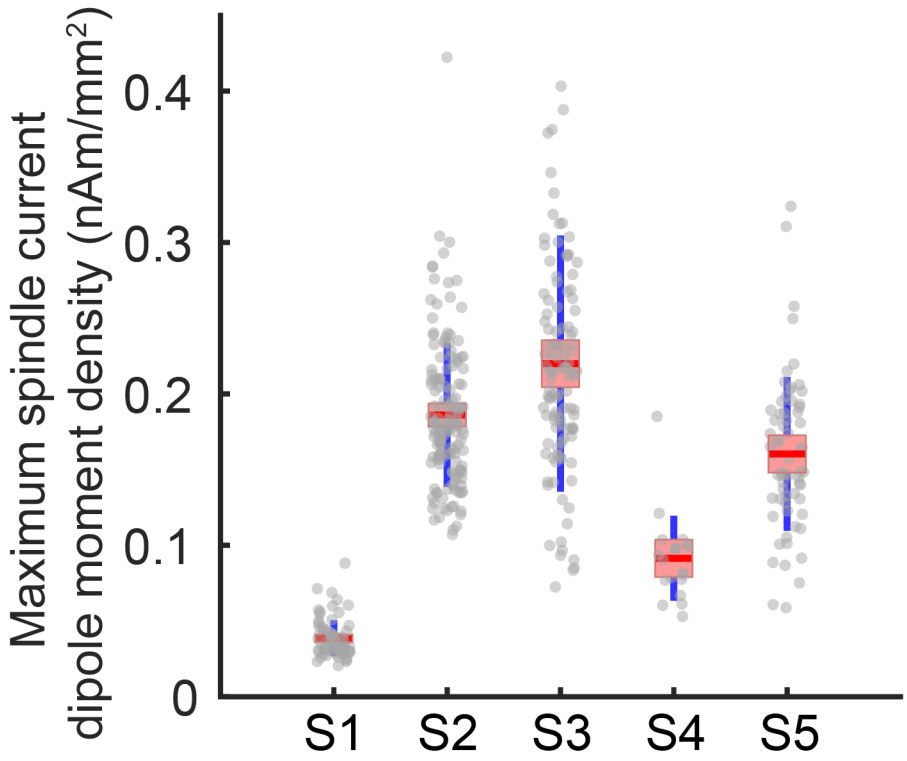

Figure 2. Maximum magnitude of sleep spindles in human laminar data. Maximum current dipole moment density estimated from CSD profiles at times of maximum 10-16 Hz power during sleep spindles. Standard deviation and 95% confidence are shown in blue and red, respectively.

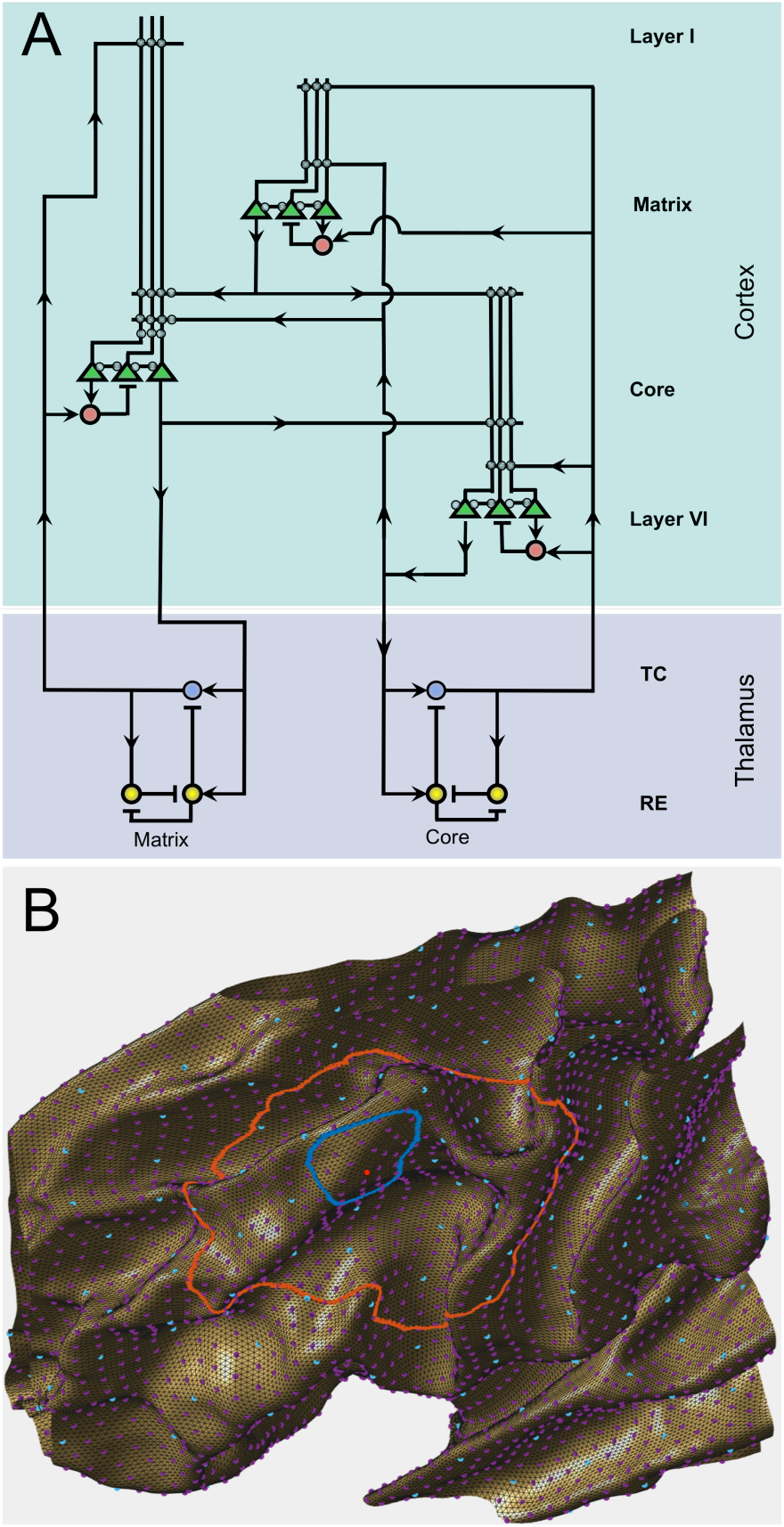
A
Layer I
Matrix
Cortex
Core
Layer VI
TC
Thalamus
RE
Matrix
Core
B

Figure 3. Network connectivity. (A) Schematic representation of thalamocortical and corticocortical connections. (B) Example of cortical geodesic-based connectivity. Pyramidal and inhibitory cortical neurons exist at purple and cyan locations, respectively. The blue contour shows the fanout of a core-projecting thalamic neuron at the virtual position marked in red. The orange contour shows the same for a matrix-projecting thalamic neuron at the same virtual location.

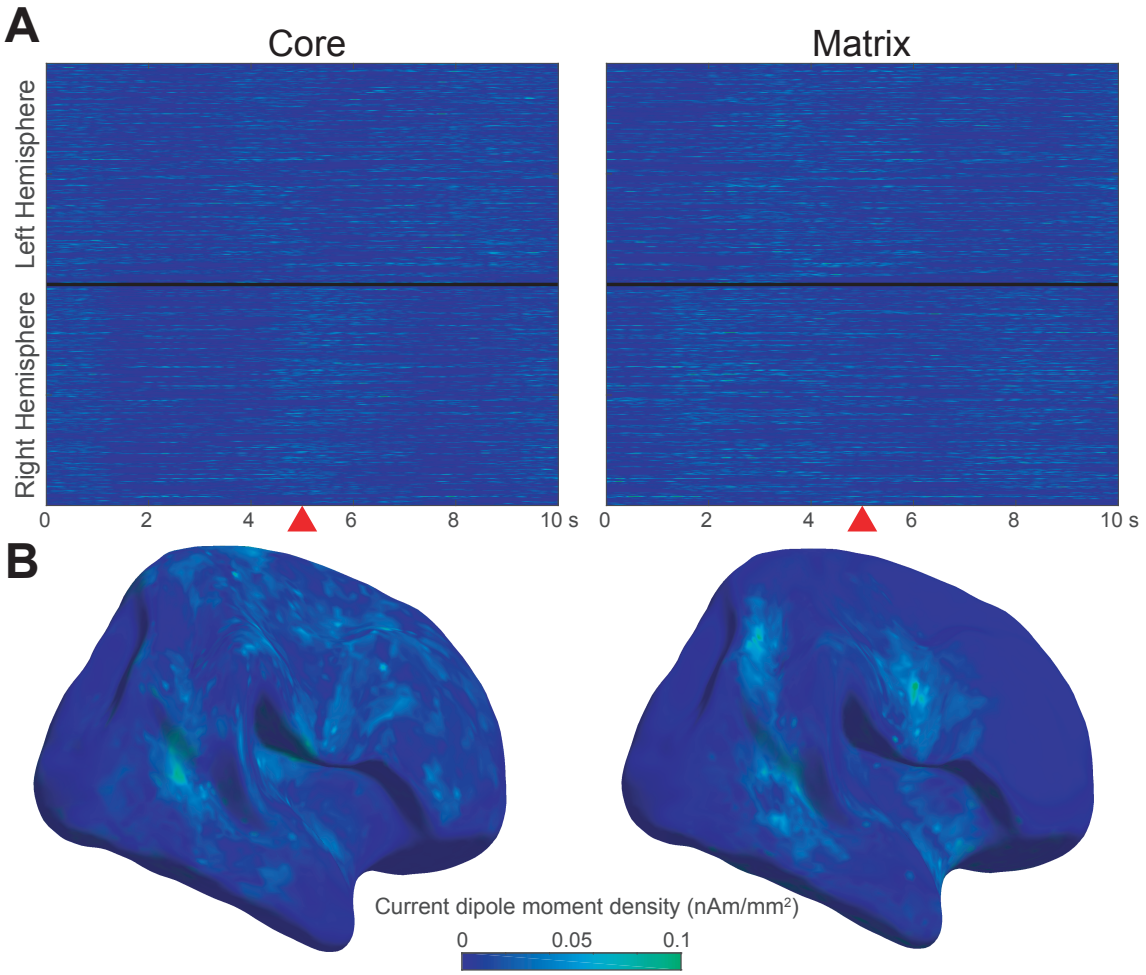

Figure 4. Simulated cortical sources. (A) 10 seconds of simulated spindling for one subject. (B) matrix and core pyramidal current dipole moment density distributed across the cortex at a single time point, marked in red. Data are displayed on an inflated right cortex.

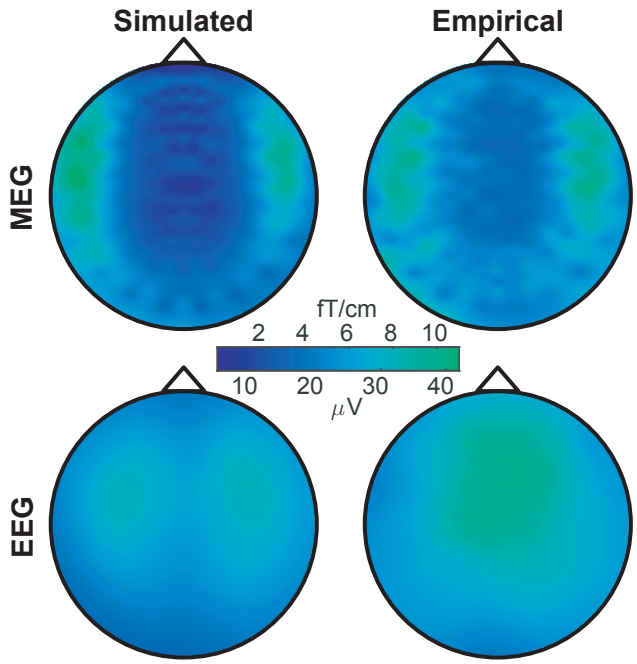

Figure 5. Grand average 10-16 Hz complex envelope topographies for empirical and simulated M/EEG during automatically detected EEG spindles. Empirical data show averages for six subjects, simulated data for six simulation runs using those subjects' cortical surfaces, cranial tissue boundaries, and M/EEG sensor positions.

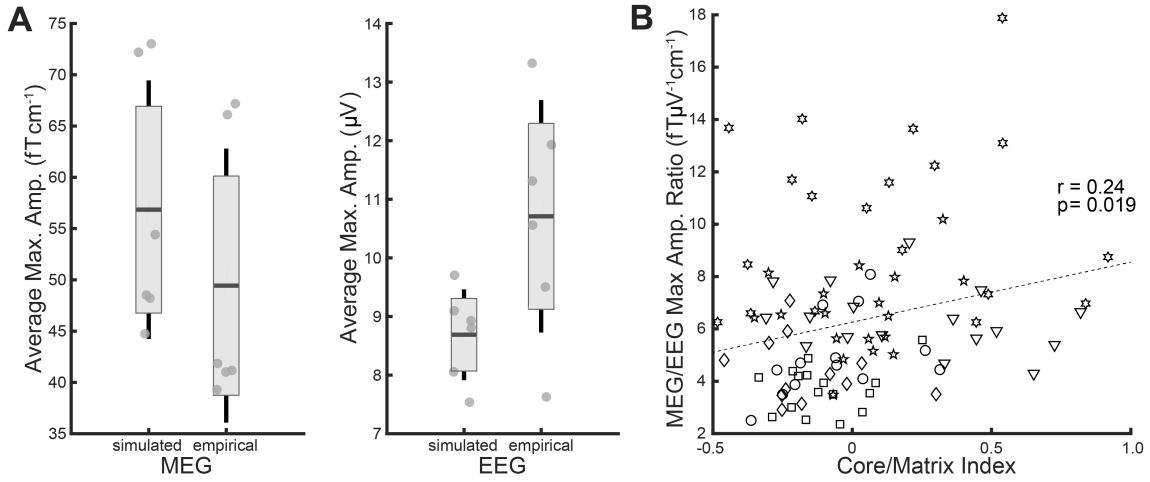

Figure 6. M/EEG sensor 10-16 Hz envelope maxima during EEG spindles. (A) For simulated and empirical M/EEG, 10-16 Hz envelopes are averaged across the duration of the spindles then averaged across spindles. The envelope magnitudes of strongest sensors are shown. (B) Simulated individual spindle sensor maxima vs. neural model derived core/matrix index. Positive index values indicate a more core-weighted spindle while negative values indicate a more matrix-weighted spindle. Each marker represents an individual simulated spindle with symbols signifying the simulation run, each using a

different donor subjects' cortical surfaces, cranial tissue boundaries, and M/EEG sensor positions.